Synthesis of Eu-doped $K_{0.5}Na_{0.5}NbO_3$ ceramics and their luminescent and dielectric properties

Marta Lubszczyk[1] · Tomasz Brylewski[1] · Krzysztof Ziewiec[2] · Andrzej Kruk[2]

Abstract

$K_{0.5}Na_{0.5}NbO_3$:xEu sol–gel powders and bulk samples were synthesized by means of a modified sol–gel method. Two types of samples were obtained via sintering at two temperatures. X-ray diffraction revealed the presence of the perovskite phase in materials obtained at both temperatures. Eu^{3+} emission and excitation studies were conducted to determine its luminescence response. For $K_{0.5}Na_{0.5}NbO_3$:xEu sinters, the excitation spectra included narrow peaks in the VIS range due to the $^5D_0$–$^7F_1$ and $^5D_0$–$^7F_2$ relaxation processes. These transitions were indicative of the presence of Eu^{3+} at sites of low symmetry. Dielectric studies indicated that Eu_2O_3 affected the observed phase transitions. The influence of sintering temperature on structure and physicochemical properties was discussed.

Keywords KNN · Wet chemistry method · Dielectric properties · Luminescence

Introduction

Ferroelectric oxide materials are an important group of materials that are widely applied in modern electronic devices owing to their unique electric properties, namely their ferroelectricity, piezoelectricity and high dielectric permittivity. The materials that are currently the most commonly used are based on $PbZrO_3$–$PbTiO_3$ solid solutions, referred to as PZT. Due to the toxicity of lead, which is the main component of PZT, it has become necessary to develop new lead-free, ferroelectric materials with similar properties [1–3]. Among the alternatives, materials based on sodium–potassium niobate ($K_{0.5}Na_{0.5}NbO_3$-KNN) have gained considerable attention due to its high piezoelectric modulus and high Curie temperature [4, 5].

Another noteworthy topic is the further functionalization of this material via doping. It has been shown that ferroelectric oxides doped with rare-earth ions can exhibit both electrical and optical (e.g., photoluminescence) properties [6–10]. Such multifunctional properties open new

possibilities in the field of optoelectronics. The integration of electrical and optical features could also reduce the cost and size of new optoelectronic devices. It should also be emphasized that dopant incorporation into the matrix of ferroelectric ceramics affects both their electrical properties and their microstructure by reducing the grain growth during sintering [11, 12]. KNN-based materials doped with several rare-earth doped ions have been studied in recent years. The reports showed improved electrical properties, including dielectric permittivity, piezoelectric modulus and remanent polarization [6, 8, 13, 14]. The incorporation of selected rare-earth elements (e.g., Sm [6], Tb and Tm [15], Gd [13], Ho [16], Nd [17]) into the KNN matrix changes its typical ferroelectric behavior into that of a relaxor-like ferroelectric and is also associated with a change in phase transition temperatures. In addition to studying the electrical properties of KNN, researchers have also evaluated the optical performance of rare-earth KNN [6–10, 18, 19]. Both downshifting [6, 20, 21] and up-conversion [18, 22] were observed for ions such as Er^{3+}, Sm^{3+}, Dy^{3+}, Eu^{3+}, Pr^{3+} and Ho^{3+}.

It should be highlighted that the preparation process has a significant impact on the final properties of the material. Ferroelectric ceramics based on sodium–potassium niobates are usually synthesized by means of the solid-state reaction method. While this method is simple and fast, it may yield powders that exhibit inhomogenous particle size

✉ Andrzej Kruk
andrzej.kruk@up.krakow.pl

1 Faculty of Materials Science and Ceramics, AGH University of Krakow, al. Mickiewicza 30, 30-059 Krakow, Poland

2 Institute of Technology, University of the National Education Commission, ul. Podchorążych 2, 30-084 Kraków, Poland

distribution and contain agglomerates. This may result in reduced electrical and optical properties of the final product. As an alternative, wet chemistry methods can also be utilized. Of the wet chemistry methods that have been successfully used for the synthesis of ferroelectric ceramics, the following are worth mentioning: co-precipitation [23], crystallization under hydrothermal conditions [24–26], and sol–gel [27–29] and Pechini [30–33] methods. These methods allow atomic-level mixtures of all components to be obtained at lower processing temperatures. In addition, the obtained powders contain nanosized grains and have the desired chemical and phase composition. The metal-chelate gel route appears to be particularly worthy of attention. This method of powder preparation is based on the use of water-soluble metal-chelate complexes. The advantages of this technique are its simplicity and versatility. For example, Kakimoto et al. [30] used a citrate precursor technique to obtain an undoped $K_{0.5}Na_{0.5}NbO_3$ ceramic which exhibited better electrical properties ($\varepsilon_r = 657$, $d_{33} = 161$ pC/N) than KNN synthesized using the solid-state reaction ($\varepsilon_r = 384$, $d_{33} = 98$ pC/N).

To the best of our knowledge, Wu et al. [22] have made the only successful attempt to obtain a KNN material doped with a rare-earth element by means of the Pechini method; the material in this case was KNN:Er. The photoluminescence intensity of the Pechini-produced KNN:Er was significantly higher than that of KNN:Er obtained via the solid-state reaction method. These effects were explained by the better homogeneity of the admixture in the host material. The afore-mentioned authors utilized a niobium precursor based on an oxalic acid complex. However, oxalic acid is known to react with lanthanides and thus form insoluble oxalates. Compounds based on oxalic acid should therefore be avoided when synthesizing materials with lanthanide elements by means of soft chemistry methods.

In this work, $K_{0.5}Na_{0.5}NbO_3$ doped with 0.05 and 0.025% Eu_2O_3 powders was synthesized using an optimized Pechini method utilizing citric acid and then sintered at 1373 K (1100 °C) and 1473 K (1200 °C). Eu_2O_3 was chosen as the dopant, since Eu^{3+} ions can be excited efficiently with ultraviolet and blue light to induce [34]. The influence of the dopant concentration and temperature of thermal treatment on the structure and the electrical as well as luminescent properties was examined. The effect of the Eu_2O_3 addition on the KNN powders was evaluated by means of XRD, SLS and SEM–EDS analyses.

Materials and methods

Powders consisting of $K_{0.5}Na_{0.5}NbO_3$ doped with 0.025 or 0.05 mol% of Eu_2O_3 were obtained via a modified Pechini method that involved the use of citric acid. A water-based niobium precursor was prepared by chelating Nb ions with citric acid, as described in a previous report [32]. Nb_2O_5 and KOH were mixed in 1:6 molar ratio and calcined for 2 h in air at 623 K to obtain water-soluble potassium niobates. Then, after dissolving potassium niobates in the distilled water, amorphous $Nb_2O_5 \cdot nH_2O$ was precipitated by using nitric (V) acid. Finally, filtered off and washed $Nb_2O_5 \cdot nH_2O$ was dissolved in citric acid solution, by mixing for several weeks, resulting in stable solution of niobium precursor. This niobium solution was then mixed with KNO_3 (Chempur, p.a. grade), $NaNO_3$ (Chempur p.a. grade), $Eu(NO_3)_3 \times 5 \cdot H_2O$ (Sigma-Aldrich, 99.9% trace metal basis) in amounts corresponding to the desired composition. The amount of citric acid in the solution was such that the metal-to-acid molar ratio was 1:3. The, thus, obtained solutions were mixed, dried and then calcinated for 4 h in air at 973 K. Synthesis scheme is shown in Fig. 1. The resulting powders were formed into pellets and then further compacted via cold isostatic pressing (CIP) under a pressure of 180 MPa. The green bodies were freely sintered for 4 h in ambient air at 1373 or 1473 K.

Table 1 lists the sample designations depending on the amount of the Eu dopant, and the temperature at which a given sample had been sintered. These designations are subsequently used to refer to each sample.

Differential scanning calorimetric (DSC) and thermogravimetric (TG) experiments were carried out simultaneously under the following conditions: sensitivity of DSC and TG: ± 1 μV m-g^1, heating rate: 10 K min^{-1}, sample mass: 13.5 mg, air flow: 50 mL min^{-1}, apparatus: Netzsch STA 449F5 Jupiter. A Pt–Rh crucible with a diameter of 14 mm and a height of 17 mm was used with α-Al_2O_3 as the standard substance. The gas evolved from the heated samples was evaluated by means of evolved gas analysis (EGA) performed using a quadrupole mass spectrometer (Netsch QMS 403D Aëolos). Thermal data were analyzed
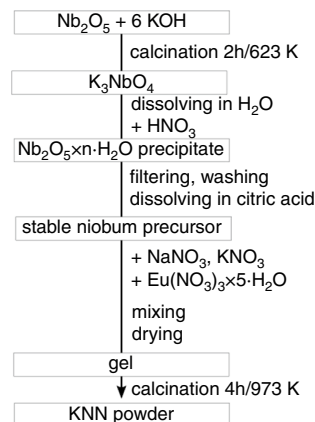

Fig. 1 Flowchart of the synthesis of KNN powder

Table 1 Sample designation

Nominal composition	Gels and powders	Sinters	
		1373 K (1100°C)	1473 K (1200°C)
0.025% mol Eu$_2$O$_3$ in KNN	KNN:Eu0.025	KNN:Eu0.025–1100	KNN:Eu0.025–1200
0.05% mol Eu$_2$O$_3$ in KNN	KNN:Eu0.05	KNN:Eu0.05–1100	KNN:Eu0.05–1200

using Netsch and OriginPro software. All of the described studies were performed in ambient air.

The morphology and microstructure of the KNN-based samples were observed using scanning electron microscopy (SEM, JEOL 6610LV, Japan). The chemical composition of the sinters was analyzed with an energy-dispersive X-ray spectroscope (EDS, Oxford), using the Aztec software.

The phase structure was examined via X-ray diffraction (Panalytical Empyrean) with Cu K-alpha radiation ($\lambda = 1.5406$ Å), over the 2θ range of 10–90°. The Panalytical X'pert High Score coupled with the PDF2 database of the International Centre for Diffraction Data (ICDD) was used for the identification of the phases present and to perform Rietveld refinement. The calculations were performed with High Score software with embedded advanced parameters but is based on the Scherrer equation:

$$D_{\mathrm{XRD}} = \frac{K\lambda}{\beta\cos\theta} \tag{1}$$

where: D_{XRD}—crystallite size [nm], λ—wavelength of X-rays (CuKα_1;λ = 0.15406 nm), cos θ—diffraction angle, $K = 0.9$, and β—corrected full width at half maximum (FWHM) of the diffraction peak.

The SALD-7500nano (Shimadzu) was used to examine the size of KNN-based particles dissolved in water by utilizing the static light scattering technique. The unit is equipped with a semiconductor laser (405 nm) and a reverse Fourier optical system.

The Archimedes method was used to evaluate the porosity and apparent density of bulk materials through hydrostatic weighing in distilled water.

The luminescence spectra were collected using the confocal laser scanning microscope (Olympus FV3000). The parameters of the method were as follows: UPLX APO 40X, numerical aperture: 0.95, objective lens and excitation beam of continuous wave laser at four wavelengths: 405, 488, and 561 nm. Depending on the wavelength range of the light source, the observed spectrum range was adjusted.

The dielectric properties of the specimens were investigated using an RLC meter (GWInstek). The unit generated a sinusoidal voltage with a 1 V peak amplitude. The complex dielectric permittivity, the loss tangent, electrical modulus were determined over a frequency range from 50 Hz to 10 MHz, as a function of ambient air temperature (from room temperature RT to 873 K with 25K step), and these conditions were also applied for impedance spectroscopy. The collected EIS spectra were analyzed with an EIS analyzer software. Field-dependent polarization was recorded for electric fields in the range of 0.1–1.0 kV mm^{-1} and a frequency of 50 Hz, with an onsite-designed Sawyer–Tower circuit. The high-voltage source was controlled manually.

Results and discussion

Thermochemical characteristics of investigated gels

The thermal behavior of the KNN:Eu0.025 and KNN:Eu0.05 gels was evaluated by means of DSC-TG-EGA, in an air atmosphere heated at a rate of 5K min^{-1}. To determine the temperatures at which different mass changes occur with better precision, the first derivative of the mass loss (dTG) was calculated and is presented as a function of temperature in Fig. 2. The evolution of the OH, NO, NO$_2$, CO, CO$_2$ gases and water was confirmed via EGA (Fig. 2). Evolution of alkali elements was measured; a very weak signal originating from KO, Na$_2$O and K$_2$O ions was detected, but it was negligible (under 10^{-10}A) and is not shown. Ions with m/z = 39, which could be attributed to NaO, were detected. However, low temperature of the detection indicated that it is rather C$_3$H$_3^+$, which could be a product of the decomposition of citric acid [35].

Thermal behavior TG–DTA of pure citric acid is presented elsewhere [36]. The DTA curve of pure citric acid exhibits two endothermic and one exothermal peaks, at 430, 473, and 683 K, respectively. The endothermic peak at 430 K is connected with the melting of pure citric acid. Another endothermic peak at 473 K is attributed to the decomposition of citric acid with a release of gases like H$_2$O and CO$_2$ accompanied with a mass loss on TG curve. One exothermic peak at temperature of 683 K arises from the combination two processes: oxidation of amorphous carbon and pyrolysis of residue organics in air.

The first interval in Fig. 2 corresponds to an endothermic peak and a mass loss of 10%, attributed to water removal (ca. 300–500 K). The following exothermic reactions are attributed to multistep decomposition process and oxidation the metal-citrate complexes, accompanied by a mass loss of
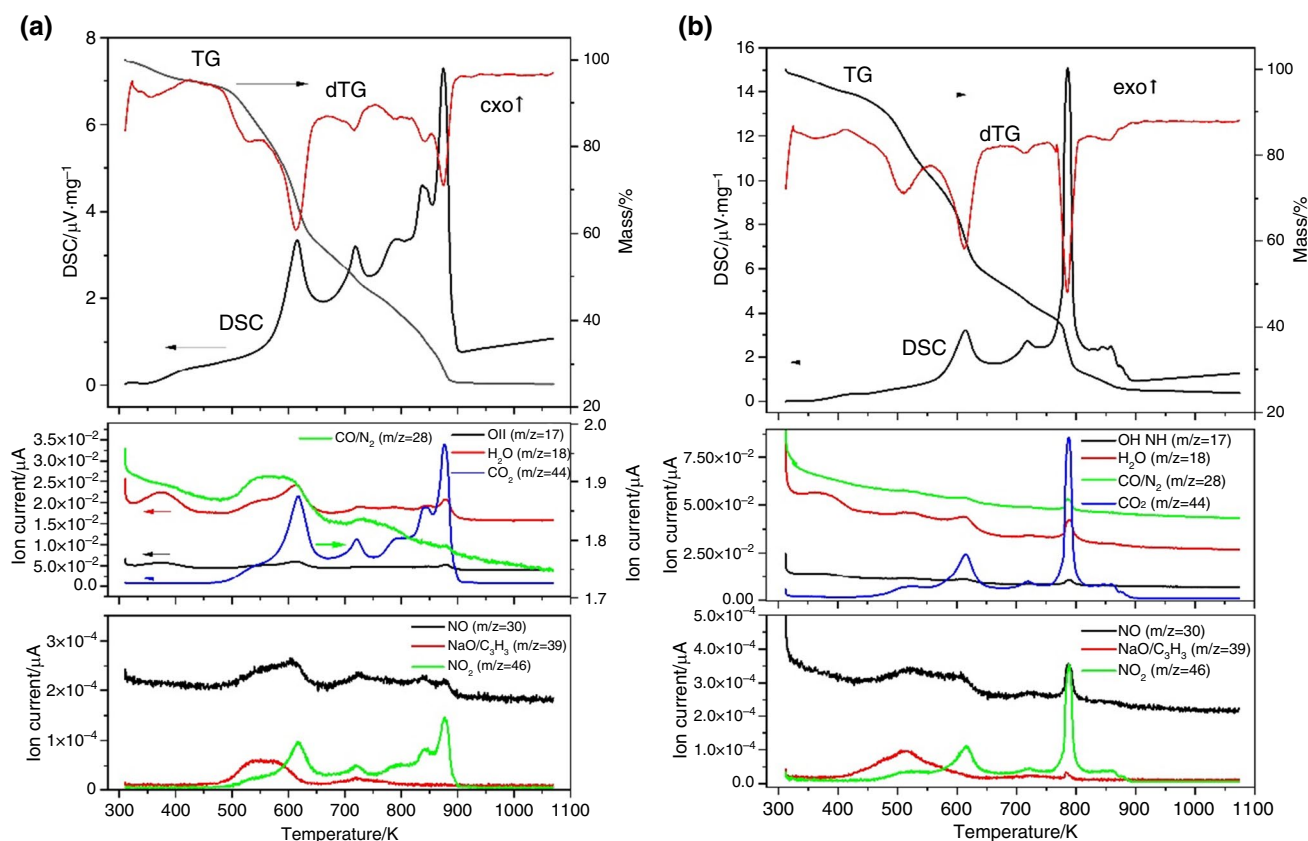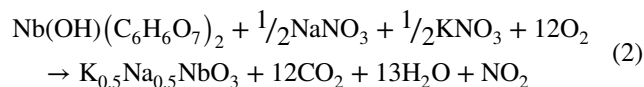
Fig. 2 DSC, TG and dTG curves recorded for the precursor gels: **a** KNN:Eu0.025 and **b** KNN:Eu0.05 and the corresponding EGA-QMS curves of gases that evolved during the thermal decomposition of the studied gels in air. Detected ions: OH ($m/z = 17$), H_2O ($m/z = 18$), CO/N_2 ($m/z = 28$), NO ($m/z = 30$), NaO/C_3H_3 ($m/z = 39$), CO_2 ($m/z = 44$), and NO_2 ($m/z = 46$)

around 50%. In this second step, two pronounced exothermic peaks can be distinguished at ca. 620 K and 720 K. Multistep decomposition behavior is normally observed for citrate-gels decomposition [37]. Decomposition of citrate complexes of metal ions in KNN:Eu may be similar to decomposition of barium and titanium citrate salts, described by Hennings and Mayr [38]. Firstly, the dehydration of citric acid led to aconitic acid, which is then decarboxylated to itaconic acid. Itaconic acid is then combusted. However, decomposition of KNN:Eu complex may run in multistep way, and also accompanied with alkali nitrate salt decomposition. Precise decomposition reaction probably involves numerous side reaction. However, total chemical reaction (Eq. 2) can be represented as follows:

$$
\begin{aligned}
&\mathrm{Nb(OH)}\left(C_6H_6O_7\right)_2 + {}^1\!/_2\mathrm{NaNO_3} + {}^1\!/_2\mathrm{KNO_3} + 12O_2 \\
&\rightarrow K_{0.5}Na_{0.5}NbO_3 + 12CO_2 + 13H_2O + NO_2
\end{aligned}
\tag{2}
$$

In the case of the KNN:Eu0.025 gel, exothermic crystallization of the KNN phase was detected at 823 K, with a small mass loss of around 3%. The decomposition of residual organic compounds adsorbed on the surface of the

solid products occurred during and after the crystallization of KNN, up to 873 K. The TG curve shows that the mass loss at 873 K was higher than at ca. 823 K. The TG and dTG curves confirm the decomposition of residue organic parts, and this was confirmed by the CO_2, H_2O, NO_2 peaks on the EGA curve (centered at 873 K).

Similar tendencies of thermochemical characteristics were observed for the KNN:Eu0.05 gel. The TG curve shows a mass loss of ~10%, which can be attributed to the elimination of gases during decomposition between 773 and 873 K. The strong exothermic peaks at 783 K and 873 K on the DSC curve for the KNN:Eu0.05gel can be attributed to the crystallization of KNN and the decomposition of the residual organic compounds, respectively. The TG data indicated a total mass loss of 76% and 71.72% for the KNN:Eu0.025 and KNN:Eu0.05 gels, respectively. The effect of Eu_2O_3 ion content on the thermal decomposition behavior of gels can therefore be concluded to be negligible.

In order to confirm that DSC exothermic peaks at the temperatures in range 773 to 873 K are related to crystallization of final KNN phase, the diffractograms of powders calcinated at 873 K were obtained. The XRD diffractogram
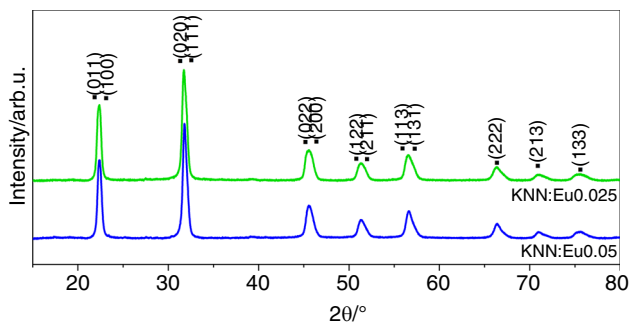
Fig. 3 XRD patterns recorded for KNN:Eu0.025 and KNN:Eu0.05 powders

Table 2 Lattice parameters and crystallite size determined for the orthorhombic Amm2 phase in KNN:Eu0.025 and KNN:Eu0.05 powders

Sample	a/Å	b/Å	c/Å	V/Å^3	Size/nm
KNN:Eu0.025	3.952	5.638	5.659	126.090	24.6
KNN:Eu0.05	3.955	5.642	5.653	126.142	24.8
pure KNN [32]	3.950	5.637	5.661	126.057	35.4

(Fig. 1S in supplementary information) verifies that both obtained powders consist primarily of perovskite-like structured K$_{0.5}$Na$_{0.5}$NbO$_3$-based materials. However, small amount of secondary phase is also present. Due to both very low content and low crystallinity of admixture phases, it is difficult to point out the nature and stoichiometry of this phase precisely. Nevertheless, after carefully check of the data available in the reference base, we suppose that these small peaks are belonging to K$_6$Nb$_{10.9}$O$_{30}$ [39]. The XRD patterns of powders calcinated at 973 K (Fig. 3) do not exhibit the presence of any secondary phase. Hence, this calcination temperature was chosen for further research.

Physicochemical characteristics of investigated powders

The influence of the Eu$_2$O$_3$ additions on the formation of the perovskite KNN phase is shown in the XRD patterns recorded for the powders calcinated at 973 K and then crushed by hand in an agate mortar (Fig. 3). The prominent XRD peaks on the curves for the KNN:Eu0.025 and KNN:Eu0.05 powders are indexed to a single orthorhombic KNN phase and its respective *hkl* planes. Table 2 lists the lattice parameters determined after Rietveld refinement had been performed for both powders to confirm phase stoichiometry as well as crystallite size values. Both KNN:Eu0.025 and KNN:Eu0.05 powders exhibited a single phase with a non-centrosymmetric A-centered orthorhombic lattice structure (KNN:Eu0.025 $R_w = 5.56\%$, KNN:Eu0.05 $R_w = 4.85\%$)

and a crystallite size equal to 24.6 and 24.8 nm, respectively. No secondary phases were present in any of the samples, which suggests that Eu$_2$O$_3$ had successfully incorporated into the crystal lattice of pure KNN.

As can be seen, the position of the Bragg peaks moves toward higher angles as Eu$_2$O$_3$ content increases, which indicates a change in the host lattice. Small differences in lattice parameters were found in the XRD pattern, leading to the conclusion that even small amounts of Eu$_2$O$_3$ affect the structure of the host, and both the lattice parameters and corresponding unit cell volume increased for higher Eu$_2$O$_3$ content. The calculated data were consistent with the lattice constants reported previously for pure KNN powders [32] and other data [23, 27].

Figure 4 shows the SEM images of the KNN powder samples doped with 0.025 or 0.05 mol% of Eu$_2$O$_3$ after 4 h of calcination in air at 973 K.

The obtained results showed that the existence of large, open-structure agglomerates composed of several nanosized particles. The size of the agglomerates varied from several to several hundred micrometers, with slightly larger agglomerates for KNN:Eu0.025. Although EDS analysis confirmed the nominal composition of K$_{0.5}$Na$_{0.5}$NbO$_3$ in both samples, the concentration of europium was too low to be detected.

The particle size distribution (PSD) curves (Fig. 5) show the appearance of single nano-sized grains and micro-sized agglomerates and/or aggregates. These results were confirmed by the performed SEM observations and XRD analyses. The PSD curves have a similar, multi-modal shape. However, the single particles of the KNN:Eu0.025 powder were smaller than those of the KNN:Eu0.05 one.

The values of PSD show that the D50 increase with Eu$_2$O$_3$ added from 0.04 to 0.12 nm. It should be noted that the agglomeration of the largest particles differed significantly for both batches. Nanosized particles create larger agglomerates due to their larger specific surface area providing more active surface sites. Hence, the KNN:Eu0.025 powder was much finer, with submicron-sized particles being predominant, as represented by its D10 value, which was half an order of magnitude lower than for KNN:Eu0.05. The results showed that for more than half of all particles, at least one dimension was below 100 nm. This behavior may produce denser sinters and may cause the KNN phase to form at lower sintering temperatures with respect to 0.05% Eu$_2$O$_3$-doped KNN.

Physicochemical properties of sinters

The KNN:Eu0.025 and KNN:Eu0.05 powders were pressed into pellets and then sintered for 4 h in air at 1373 K (1100°C) and 1473 K (1200 °C). The microstructure and chemical composition of the obtained ceramics were examined via SEM/EDS analysis. The SEM micrographs of the
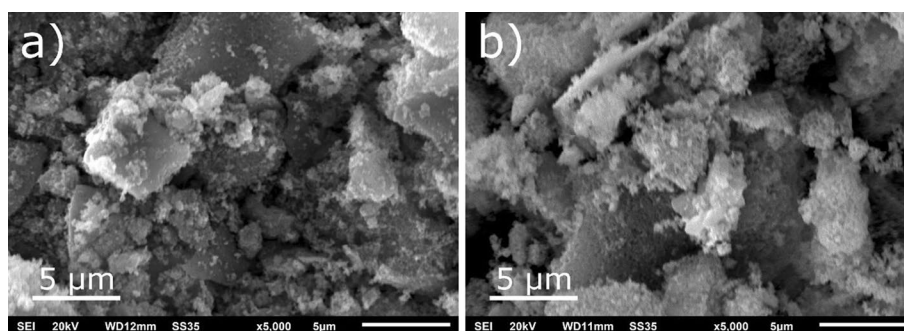
KNN:Eu0.025–1100 and KNN:Eu0.05–1100 sinters (Fig. 6a and b) revealed their homogeneous microstructure with well-developed cuboidal grains. The size of grains ranged from 1 μm to 5 μm, and pores were located at grain boundaries. EDS analysis showed that the distribution of all elements in the sinters was homogenous and that the desired stoichiometry had been obtained. Nearly no undeveloped grains were observed. The KNN:Eu0.025–1200 and KNN:Eu0.05–1200 (Fig. 6c and d) exhibited a different microstructure with regions of higher and lower density. In regions with significant porosity, well-shaped hexagonal grains with a size in the range of 4–25 μm can be observed. In regions with higher density these grains formed a continuous matrix that had likely been formed as result of the simultaneous growth of grains due to the material's overmelting. The walls of grains in the powdered sintered at 1473 K were larger and more developed, with sharp edges. It can be noted that individual grains had formed traverses.

A detailed analysis of the EDS element distribution maps taken for the denser regions of the powder sintered at 1373 K revealed discrete areas rich in sodium as well as areas with high potassium conten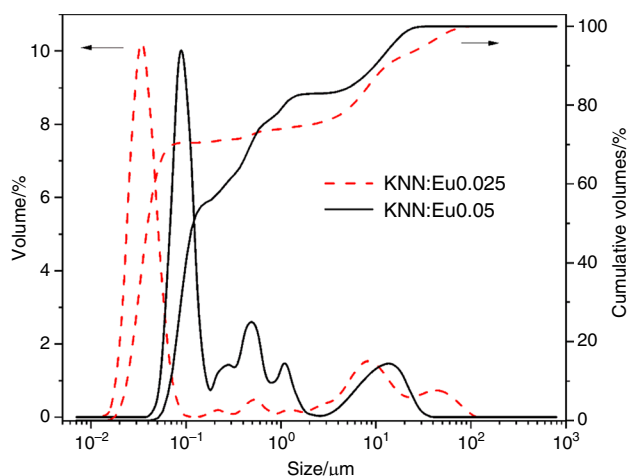t (Fig. 7a). Two niobate phases can be distinguished in these maps—a predominant phase containing mostly sodium and a small amount of potassium and another phase with a continuous matrix; the latter was composed mostly of potassium. The average element content determined for the samples sintered at 1473 K based on the EDS analyses indicated smaller amounts of potassium (Fig. 7b).

Literature data indicate that increased inhomogeneity and deviations from stoichiometry in sodium–potassium niobates are associated mostly with the evaporation of sodium rather than potassium [40–42]. On the other hand, thermodynamic calculations show that the vapor pressure of potassium is higher than that of sodium. This is consistent with the fact that the melting point of $KNbO_3$, which is equal to 1312 K [43], is significantly lower than that of $NaNbO_3$ – 1695 K [44]. The segregation of sodium and potassium in the investigated samples, which had also been confirmed by a number of research teams [41, 45, 46], can be explained by the precipitation of the liquid phase during sintering. The phase diagram for the $KNbO_3$-$NaNbO_3$ shows that $K_{0.5}Na_{0.5}NbO_3$ undergoes incongruent melting. After passing the solidus line during thermal treatment, KNN decomposes into a potassium-rich liquid phase and a solid phase with a predominant sodium fraction. After cooling, the sinter in question becomes chemically inhomogeneous. The decrease in the potassium concentration in the sample due to evaporation is accompanied by a fall in the solidus temperature [44, 47]. The presence of a significant amount of the liquid phase also favors grain growth, including abnormal growth. This explains the fact that coarsening is observed to a higher degree than densification and also explains the increased grain size in samples sintered at 1473 K.

Figure 8 shows the X-ray diffraction patterns recorded for the KNN:Eu0.025–1100 and KNN:Eu0.05–1200. The patterns for all samples correspond to the intensity and positions of a structure isomorphic with the KNN perovskite. An analysis of the intensity of the peaks around $2\Theta = 45.5°$ leads to the conclusion that if the first peak is higher, the dominant KNN phase is orthorhombic with the space group Amm2. However, the SEM/EDS spectroscopy results indicate that the dominant KNN phase for the ceramics sintered at 1473 K

Fig. 5 Particle size distribution (PSD) and cumulative volume curves for KNN:Eu0.025 and KNN:Eu0.05 powders

Fig. 6 SEM micrographs of fracture cross sections of: **a** KNN:Eu0.025–1100, **b** KNN:Eu0.05–1100, **c** KNN:Eu0.025–1200 and **d** KNN:Eu0.05–1200
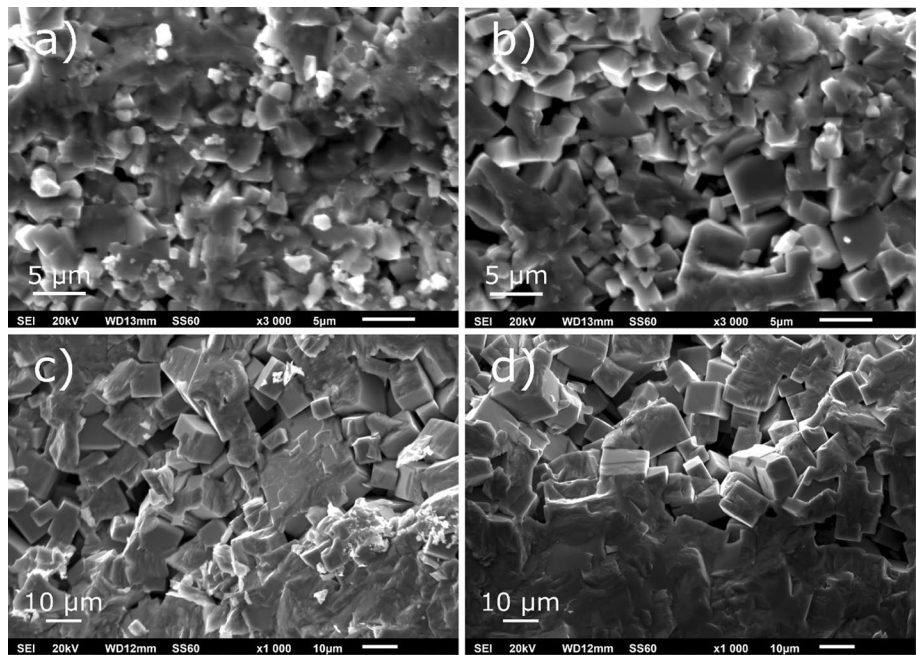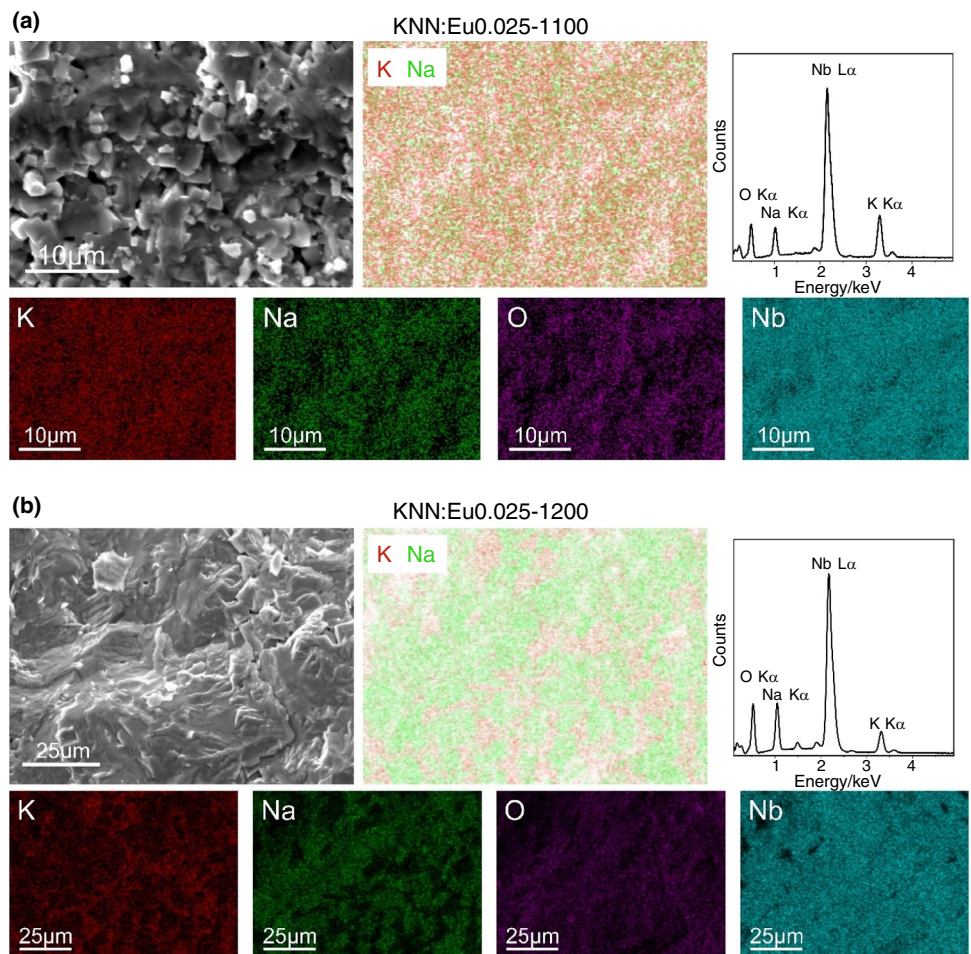

Fig. 7 SEM micrographs, point analyses, and EDS maps showing the distribution of Nb, K, Na and O in the following sinters: **a** KNN:Eu0.025–1100 and **b** KNN:Eu0.025–1200

should not be orthorhombic with $K_{0.5}Na_{0.5}NbO_3$ stoichiometry, but rather monoclinic $K_xNa_{1-x}NbO_3$ (where x < 0.5). These sinters also contained a secondary phase, for which peak positions can be attributed to a tungsten bronze-type structure of potassium niobate – $K_6Nb_{10.9}O_{30}$ [39].

The results of Rietveld refinement performed for the studied sinters are listed in Table 3 and include the lattice parameters and theoretical density of the investigated sinters as well as the mass fractions of individual detected phases. In the case of the KNN:Eu0.025–1100 and KNN:Eu0.05–1100 samples, the orthorhombic $K_{0.5}Na_{0.5}NbO_3$ phase with the space group Amm2 [48] was found. For the KNN:Eu0.025–1200 and KNN:Eu0.05–1200 sinters, monoclinic $K_{0.3}Na_{0.7}NbO_3$ with the space group Pm [49] was observed. The secondary phase of the sinters was established to be tetragonal $K_6Nb_{10.9}O_{30}$ with the group P4/mbm [39]. The unit cell parameters of the KNN phase decreased with increased Eu_2O_3 content. The ionic radius of Eu^{3+} (coordination number (CN) = 8, ionic radius (R_i) = 1.07 Å) is smaller than those of K^+ (CN = 12, R_i = 1.64 Å) and Na^+ (CN = 12, R_i = 1.39 Å) and larger than that of Nb^{5+} (CN = 6, R_i = 0.64 Å) [50]. Thus, Eu^{3+} ions occupy the A-position in the ABO_3 perovskite unit cell, replacing sodium and potassium, which causes the unit cell to shrink. The A-site substitution of europium, resulting in a donor doping effect, can be represented by the following equation:

$$Eu_2O_3 \xrightarrow{KNN} 2Eu^{..}_{Na/K} + 4V'_{Na/K} + 3O_O \qquad (3)$$
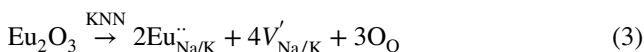
The bulk densities of KNN:Eu0.025–1100 and KNN:Eu0.05–1100 samples were 4.11 and 4.02 g cm^{-3}, respectively, whereas the corresponding values for the KNN:Eu0.025–1200 and KNN:Eu0.05–1200 sinters were equal to 3.97 and 4.03 g cm^{-3}, respectively. The apparent density of the sinters containing 0.025 mol% of Eu_2O_3 decreased considerably as sintering temperature increased, while the apparent density of the KNN:Eu0.05 sinters increased slightly. Similar tendencies had been observed earlier for KNN ceramics for which a liquid phase precipitates during the sintering process [42, 51]. To underline these differences in the density of sinters for which phase composition changes after thermal treatment, relative density was determined based on theoretical density. The theoretical density of the sinters (d_{XRD}) was determined based on the XRD data listed in Table 3. The relative density of the KNN:Eu0.025–1100 and KNN:Eu0.05–1100 samples was equal to 90.8 and 88.8%, respectively, while its values for KNN:Eu0.025–1200 and KNN:Eu0.05–1200 were equal to 86.2 and 87.3%, respectively. The conclusion from these data is that the density of the sinters was lower for higher thermal treatment temperatures. This fact suggests that for higher sintering temperatures, grain growth was more prevalent than densification. In addition, the drop in the relative density of the samples obtained at the higher of the two temperatures might have been caused by a more intense evaporation of alkali elements.

Figure 9 shows the emission spectrum of the KNN:Eu0.05–1200 sinter after excitation with continuous light with a wavelength of 405 nm. Eu^{3+} ions were the emission center in the KKN sinter, with a main transition peak at ca. 610 nm. Three characteristic luminescence peaks of Eu^{3+} were observed in the visible region at 590, 609, 625 nm and can be attributed to the $^5D_0–^7F_1$, and $^5D_0–^7F_2$, transitions. It is known that the $^5D_0–^7F_1$ transition originates from a magnetic dipole transition, and $^5D_0–^7F_2$ is related to an electrical dipole transition [34]. The intensity of luminescent emissions is strongly dependent on the local symmetry of the Eu^{3+} ions and the properties of the neighbor ions (ligands). Eu^{3+} ions replace the Na/K ions in the host crystal structure of KNN out of symmetry, because red light ($^5D_0–^7F_2$,) is dominant.

The temperature-dependent variations in complex dielectric permittivity ($\varepsilon = \varepsilon' + i\varepsilon''$, i – imaginary number) at different frequencies for KNN:Eu0.025–1100, KNN:Eu0.05–1100, KNN:Eu0.025–1200 and KNN:Eu0.05–1200 samples are shown in Fig. 10.

Two dielectric permittivity peaks associated with different types of phase transition in KNN-type materials can be seen. The first point (P1) corresponds to the transition from orthorhombic to tetragonal, while the second one (P2) corresponds to the transition from a ferroelectric tetragonal phase to a paraelectric cubic one, respectively. The dielectric studies showed low values of the dielectric constant for all investigated samples in a low-temperature range. The maximum values of complex dielectric permittivity were observed at the highest peaks corresponding to points P1 and P2, and they are listed in Table 4. Generally, the dielectric constant increases with an increase in frequency across the entire temperature range. The evolution of ε for the KNN sinters as a function of temperature during heating and cooling processes at a given frequency is shown in an inset in Fig. 10. The KNN samples exhibited slightly higher values during cooling. The observed shifts of the P1 and P2 points can be explained by a difference in the microstructure and thermal hysteresis [52]. It was concluded that the highest ε values for KNN:Eu0.025–1100 sample are observed when a combination of dense microstructure, uniform grain size and single-phase composition occurs. The P1 temperature increased with the sintering temperature of the sample.

The results show that the first transition occurs below 473 K for the samples sintered at 1373 K, and above this temperature for the KNN samples sintered at 1473 K. This is different in the case of the P2 transition, where a higher sintering temperature causes a decrease or increase in the P2 temperature for the KNN:Eu0.025 and KNN:Eu0.05 sinters, respectively.
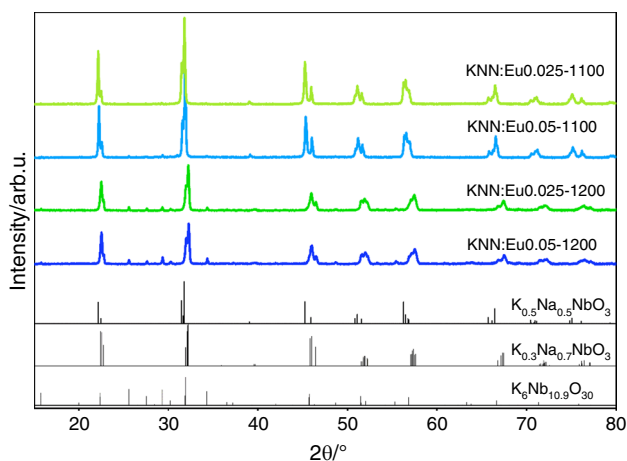
Fig. 8 XRD patterns recorded for KNN:Eu0.025–1100, KNN:Eu0.05–1100, KNN:Eu0.025–1200 and KNN:Eu0.05–1200

The influence of Eu$_2$O$_3$ content on ε is clearly visible. As can be seen in Fig. 10, the two KNN:Eu0.025 sinters generally present higher values of dielectric permittivity than KNN:Eu0.05 sinters across the entire temperature range. Eu$_2$O$_3$ affects the temperature at which phase transitions occur, shifting it toward lower values at higher concentrations. Given the same Eu$_2$O$_3$ concentration in the host material, the shifts of points P1 and P2 are evidently more pronounced for the sintering temperature of 1473 K. As can be seen, in the KNN:Eu0.05–1200, the P1 point is diffused and the maximum cannot be distinguished accurately, whereas the P2 point is sharp and relatively well-defined. Both KNN:Eu0.025–1200 and KNN:Eu0.05–1200 samples showed a strong shift of the P2 point toward higher temperatures at high frequencies. The ceramic gradually transforms from a 'normal' phase to a diffuse one with increasing sintering temperature. This is a consequence of the presence of other phases in the sinters. This was confirmed by applying the Curie–Weiss law, which can be presented as follows:

$$\mathrm{Ln}\left(1/\varepsilon - 1/\varepsilon_{\mathrm{m}}\right) = \gamma\mathrm{Ln}\left(T - T_{\mathrm{C}}\right) + \mathrm{Ln}C \qquad (4)$$

where ε_{m}—the maximum value of the dielectric constant, T_{c}—the phase transition temperature, and C—the Curie-like constant. The γ parameter is the slope of the best-fitted straight line in the graph.

The values of the γ parameter and the Curie–Weiss plots for the KNN:Eu0.025–1100 and KNN:Eu0.025–1200 sinters, recorded for a frequency of 50 kHz, are shown in Fig. 11.

The value of γ for ferroelectric materials is typically 1, but for an ideal relaxor material $\gamma = 2$. This parameter decreased with increasing sintering temperature, but it remained close to 1. The effect of the concentration of dopant ions on the dielectric properties was therefore less pronounced than that of the microstructure.

The influence of Eu$_2$O$_3$ concentration and sintering temperature was also observed in Fig. 12, in which the loss tangent (tanδ, where $\delta = \varepsilon$''/ε') of KNN:Eu0.025–1100, KNN:Eu0.025–1100, KNN:Eu0.025–1200 and KNN:Eu0.05–1200 sinters is displayed as a function of temperature.
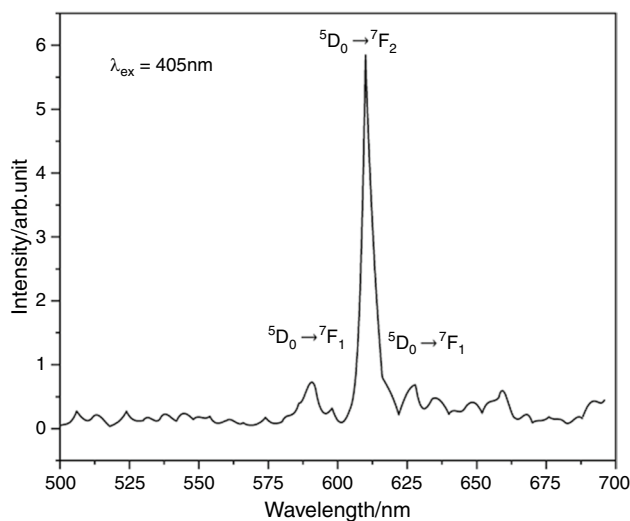

Fig. 9 Luminescence spectrum of the KNN:Eu0.05–1200 sinter after excitation with continuous light with a wavelength of 405 nm

Table 3 Rietveld refinement results for KNN:Eu0.025–1100, KNN:Eu0.05–1100, KNN:Eu0.025–1200 and KNN:Eu0.05–1200 sinters

Sample	a [Å]	b [Å]	c [Å]	V [Å^3]	d_{XRD} /g cm^{-3}	Mass fractions of detected phases
KNN:Eu0.025–1100	3.944	5.643	5.671	126.216	4.53	100%: *Amm2* K$_{0.5}$Na$_{0.5}$NbO$_3$ wR = *9.0%*
KNN:Eu0.05–1100	3.944	5.642	5.670	126.177	4.53	95.5%: *Amm2* K$_{0.5}$Na$_{0.5}$NbO$_3$ 4.5%: *P4/mbm* K$_6$Nb$_{10.9}$O$_{30}$ wR = 9.2%
KNN:Eu0.025–1200	5.596	3.905	5.569	121.685	4.60	85.2%: *Pm* K$_{0.3}$Na$_{0.7}$NbO$_3$ 14.8%: *P4/mbm* K$_6$Nb$_{10.9}$O$_{30}$ wR = 6.3%, β = 89.77 deg
KNN:Eu0.05–1200	5.590	3.901	5.559	121.223	4.62	64.1%: *Pm* K$_{0.3}$Na$_{0.7}$NbO$_3$ 35.9%: *P4/mbm* K$_6$Nb$_{10.9}$O$_{30}$ wR = 5.8%, β = 89.86 deg
pure KNN [32]	3.043	5.644	5.669	126.17	4.524	

Fig. 10 Temperature and frequency variation of dielectric permittivity (ε) for: **a** KNN:Eu0.025–1100, **b** KNN:Eu0.05–1100, **c** KNN:Eu0.025–1200 and **d** KNN:Eu0.05–1200 sinters. Inset: ε(T) function during heating/cooling at a frequency of 1 MHz
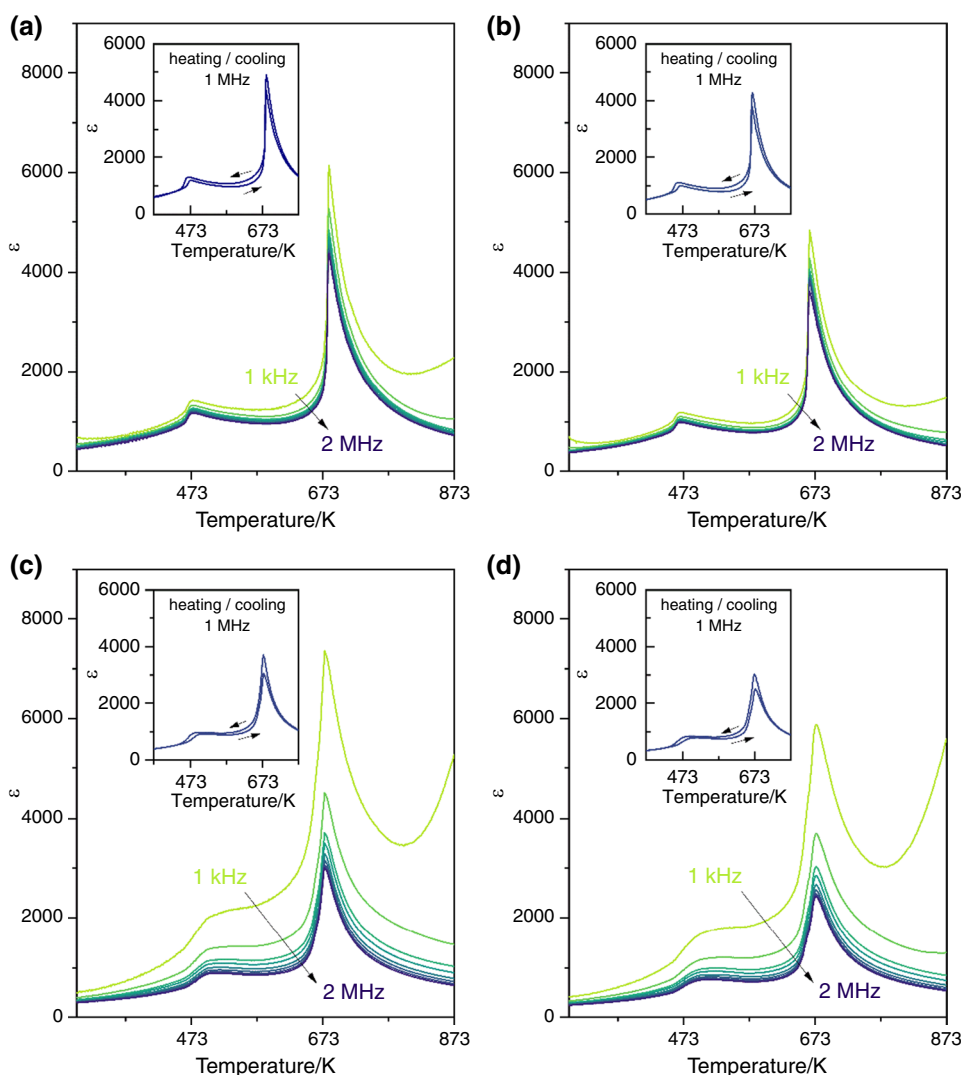
For all specimens, tanδ shifted toward higher values when temperature increased and frequency decreased. The loss tangent showed strong dispersion, especially in the high-temperature range.

The increase in the tanδ values around P1 was almost negligible. Nevertheless, the values of tanδ around P2 rose significantly, and the shape of tanδ peaks became sharp

due to the increased tetragonal phase fraction. However, higher Eu_2O_3 content was associated with a decrease in the temperature at which points P1 and P2 had appeared. Moreover, an increase in tanδ was observed for both phase transitions when dopant level increased. The values of the static dielectric constant of all samples were similar because of the same concentration of oxygen vacancies, which generated the same number of harmonic oscillations. The reason for this abnormal tanδ rise was the presence of different phases forming under different vapor pressures and diffusion velocities of sodium and potassium during the thermal treatment. Other reasons included direct current conduction, space charge migration (interfacial polarization contribution), and dipole loss from movement of the molecular dipoles.

Figure 13 and Fig S2 (in the supplementary part) show the evolution of dielectric permittivity (ε) of the KNN:Eu0.05–1200 and other samples during measurement with applied ac voltage from 0.01 mV to 2 V for
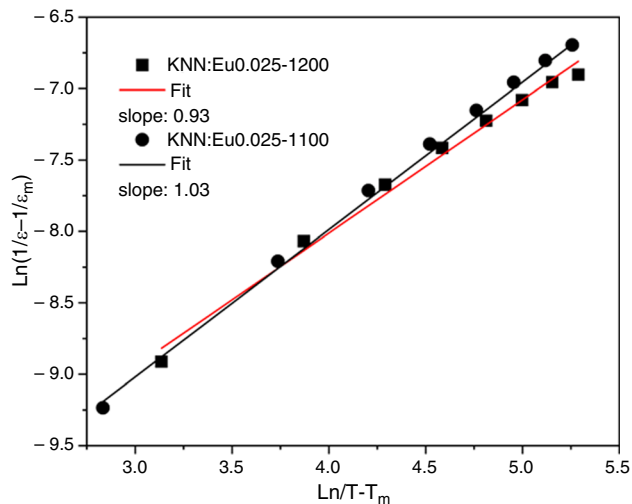
Table 4 Maximum values of dielectric permittivity for KNN:Eu0.025–1100, KNN:Eu0.05–1100, KNN:Eu0.025–1200 and KNN:Eu0.05–1200 sinters at selected temperatures, determined at a frequency of 0.5 MHz and a voltage of under 1 V

Sample	P1	P2
KNN:Eu0.025–1100	T = 475 K ε = 1203	T = 682 K ε = 4453
KNN:Eu0.05–1100	T = 468 K ε = 1005	T = 664 K ε = 3887
KNN:Eu0.025–1200	T = 498 K ε = 940	T = 675 K ε = 3152
KNN:Eu0.05–1200	T = ~493 K ε = 800	T = 474 K ε = 2562

Fig. 11 Plots representing the dependence Ln(1/ε-1/ε_m) for the KNN:Eu0.025–1100 and KNN:Eu0.025–1200 as a function of Ln(T-T$_m$)

selected frequencies. The dielectric properties of the KNN:Eu samples show little AC voltage dependence.

The dielectric permittivity evolution as function of frequency at selected applied voltage is presented as the inserts in Fig. 13. The maximal permittivity ε_{max} does not change significantly with applied measuring voltage for all samples.

Generally, dielectric permittivity values decrease with the increasing frequency undergoing an exponential decay. The anomaly phenomenon is observed in the low-temperature region between 633 and 673 K due to the presence of the additional relaxation process.

EIS analyses were conducted to investigate the dielectric properties of the KNN:Eu0.025–1100 sample. Impedance spectroscopy was used to determine the contribution of resistivity from the bulk and the grain boundaries in the studied sinter. The imaginary part (Z'') of impedance curves as a function of real parts (Z') was measured using the RLC meter at selected temperatures. As shown in Fig. 14, the Nyquist plots consist of a quasi-semicircle similar to a semi-ellipse.

The magnitude of Z' vs. Z'' decreases with increasing temperature for all samples, as expected with dielectrics. Total impedance (R_T) was calculated as the sum of the grain resistivity (R_G) and the grain boundary resistivity (R_{GB}) at low and high frequency ranges, respectively. The presence of a single semicircle indicates that the grain resistivity of the material had a dominant contribution to the total impedance. Non-separated semi-arcs were observed due to the similar time constant of R_G and R_{GB}. In order to trace the changes in the EIS spectra of

KNN:Eu0.025–1100 during heating, the equivalent electrical circuits (EECs) shown in Fig. 14 were applied.

An analysis of the corresponding Nyquist plot shows that the applied EEC is a very adequate representation of the impedance data for this sinter. The R_G and R_{GB} elements represent the grain and grain boundary resistivity, respectively. The temperature dependences of EIS data— including R_G, R_{GB} and R_T—are shown in Fig. 15.

Higher conductivity is associated with higher frequency of charge carrier hopping between ions. The energy of activation (E_a) of KNN:Eu0.025–1100 sinter was calculated based on a modified Arrhenius equation, expressed as follows:

$$R = R_0 \exp\left(-\frac{E_a}{kT}\right) \tag{5}$$

where: R_0-pre-exponential factor representing the high-temperature limit of conduction.

The total activation energy for the KNN:Eu0.025–1100 sinter was equal to 1.35 eV. The activation energy of R_G (1.12 eV) is lower than that for R_{GB} (1.21 eV) in the temperature range from 673 to 873 K. The obtained values clearly suggest that the conductivity of grains is higher than that of grain boundaries and confirm a thermally activated process. The results show that the charge carrier hopping is the predominant mechanism of electrical conduction.

The frequency evolution of the real and imaginary parts of the EIS spectra recorded for the KNN:Eu0.025–1100 sinter at higher temperatures (773–873 K) is presented in Fig. 16.

In the imaginary Z'' plot, a single peak can be seen, which is typical of pure KNN materials and suggests the dielectric relaxation process. Temperature-dependent relaxation in the investigated ceramic materials was confirmed by the expansion of the peak with temperature. As can be seen, the maxima of the curves shift toward lower frequencies at lower temperatures. The relaxation frequency shifted to higher values when the sample was being heated. Both the delayed relaxation of space charge and faster recombination at high frequencies intensified at increased temperatures.

The frequency evolution of the electric modulus of the KNN:Eu0.025–1100 sample—M' and M''—at selected temperatures can be seen in Fig. 17.

Only a single relaxation peak can be seen in the M'' dependence. The M'' of this sinter increased with frequency, reached a maximum (M''_{max}) at a certain point, and then decreases. At the same time, the maximum peak shifted toward higher frequencies as the KNN samples is heated. This behavior confirmed a decrease in the relaxation time and also indicated that the dielectric relaxation process was thermally activated because of electron hopping [53]. Figure 17 also shows that M increased with

Fig. 12 Temperature and frequency variation of dielectric loss tangent for: **a** KNN:Eu0.025–1100, **b** KNN:Eu0.025–1100, **c** KNN:Eu0.025–1200 and **d** KNN:Eu0.05–1200 sinters
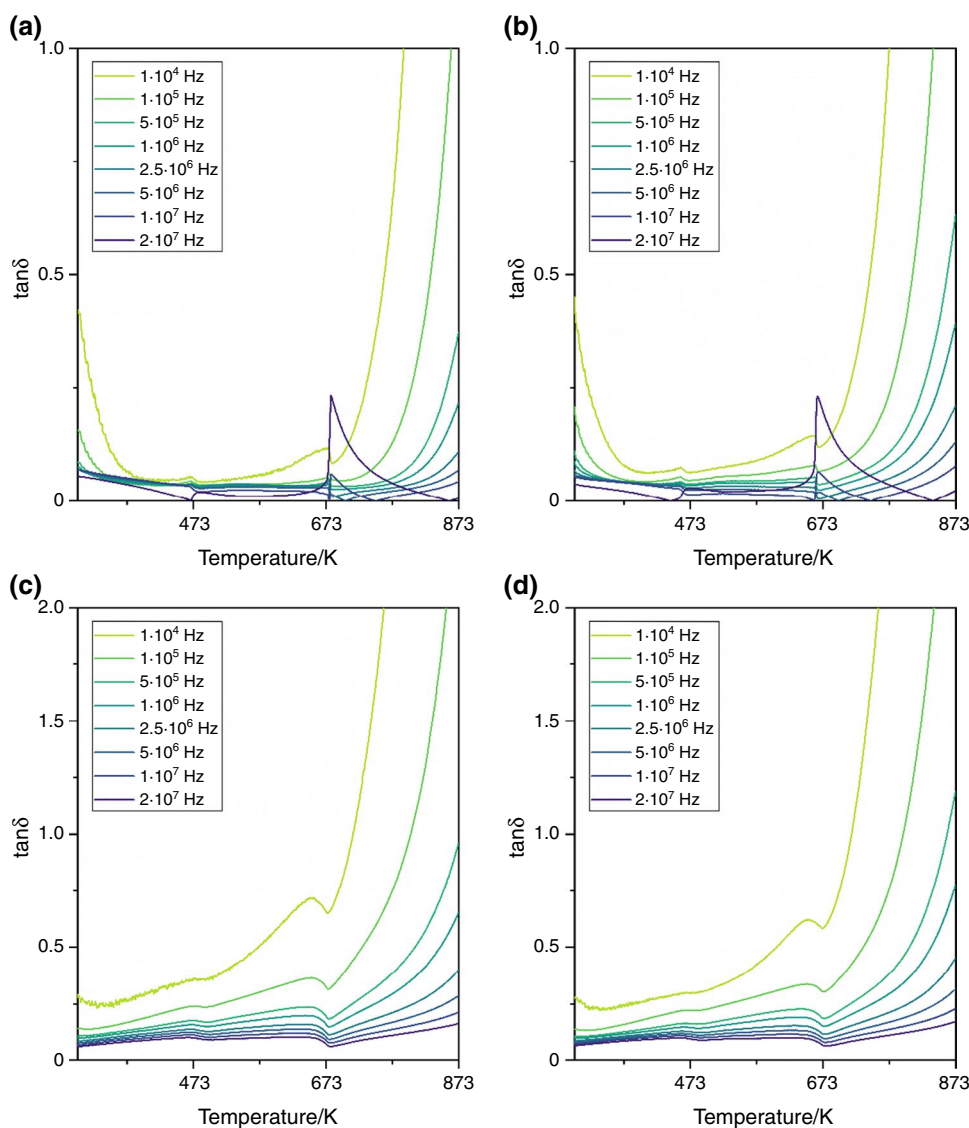
increasing frequency. The real part of the electric modulus peak shifted toward higher frequencies and at the same time, the peak became more narrow. The sample thus clearly exhibits dispersion.

The relaxation time (τ) was calculated from the maximum value of M'' as a function of frequency and is given by the relation [54]:

$$\tau = 1/2\pi f \tag{6}$$

where: f—the frequency of relaxation in maximum point of M''. This relation is presented in Fig. 3S (the supplement part).

The value of E_a estimated from the Arrhenius equation for the KNN:Eu0.025–1100 sample was 2 eV (See supplement).

The Cole–Cole diagram of the complex dielectric modulus M (the imaginary M'' as a function of the real M' parts)

determined for the KNN:Eu0.025–1100 sample at selected temperatures is shown in Fig. 18.

Each curve is represented by a single semicircle, and all curves are complete. This semi-arc shape indicates that the effect of grain boundaries was more significant than the effect of grains in the conduction process. Grain resistance only became significant in the conduction process below 723 K, which is manifested as a distortion in the high frequency region (right side of the arc). The area under the arc decreased with decreasing temperature, confirming a thermally activated process. The shift of the center of the semi-arcs toward lower M' values represents a decrease in capacitance. It can be explained as follows—increasing temperature produced new vacancies and shifted the equilibrium center positions of the cations and, in consequence, led to a decreased relaxation time of the specimen. Semi-circles
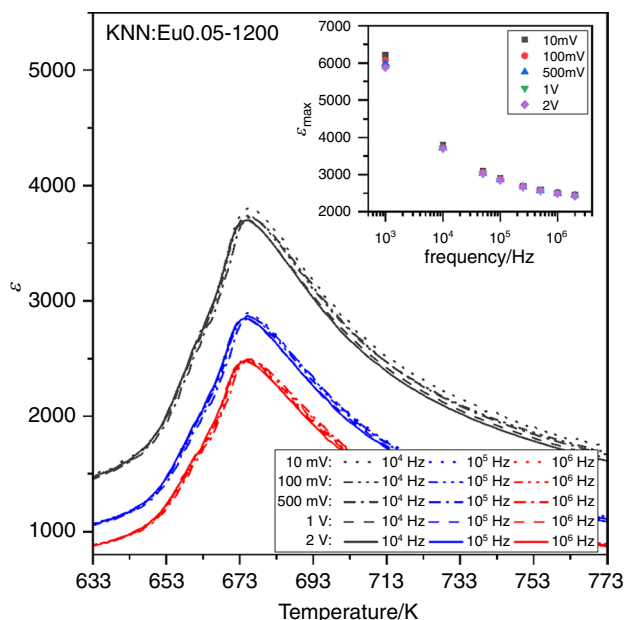
Fig. 13 Temperature dependence of electric permittivity ε for KNN:Eu0.05–1200 measured for different AC field amplitudes and selected frequencies. Inset: maximum dielectric permittivity as a function of frequency at different applied AC voltage
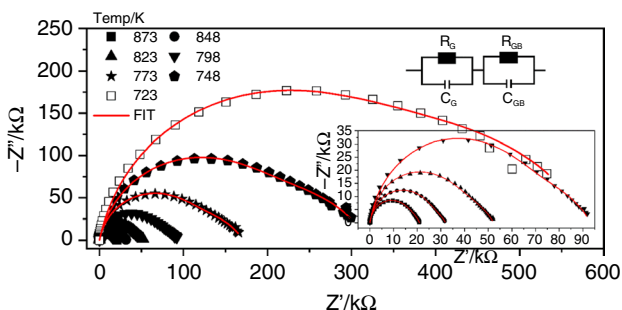

Fig. 14 Nyquist plot for the KNN:Eu0.025–1100 sinter at different temperatures between 723 and 873 K. Inset: the equivalent electrical circuit model

Fig. 15 Arrhenius plot representing the resistivity of the KNN:Eu0.025–1100 sinter. Markers indicate experimental points, and the solid line is the line fit
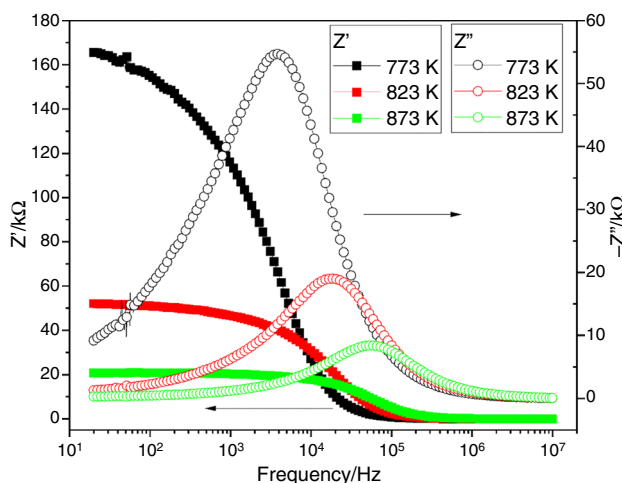
Fig. 16 Frequency dependences of Z' and Z'' for the KNN:Eu0.025–1100 sinter at selected temperatures

become incomplete as typical relaxation phenomena disappear, and non-Debye relaxation is generated.

The KNN:Eu0.025–1100 sinter was selected for ferroelectric measurements. The studies were conducted under an electric field of 15 kV cm^{-1}. The polarization (P) of this sample vs. the electric field (E) measured over a range from room temperature to 648 K and with a 25 K step is shown in Fig. 19.

Well-saturated P-E loops confirmed a typical ferroelectric nature across the entire temperature range. Under the same voltage, the KNN:Eu0.025–1100 ceramic material exhibits a lower coercive field and higher remanent

polarization than the pure KNN ceramic obtained in the same way, for which the corresponding values were 18 μ C cm^{-2} and 10 kV cm^{-1} [32].

Figure 20 presents the temperature dependence of P and E of the KNN:Eu0.025–1100 sample across the entire measurement range.

The following figure shows a global minimum at the temperature around 498 K. It can be seen that the intensity of the P_r and E_c decreased with an increasing temperature up to P1 point, where the phase transition takes place. Again, P_r and E_c parameters reached their maximum values at the highest temperatures, since the tetragonal-to-cubic phase transition causes the polarization state to be unstable, which is why
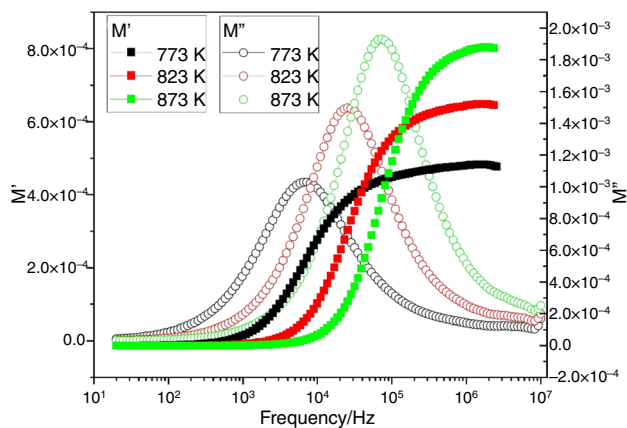
Fig. 17 Frequency dependencies of M' and M'' for the KNN:Eu0.025–1100 sinter at selected temperatures
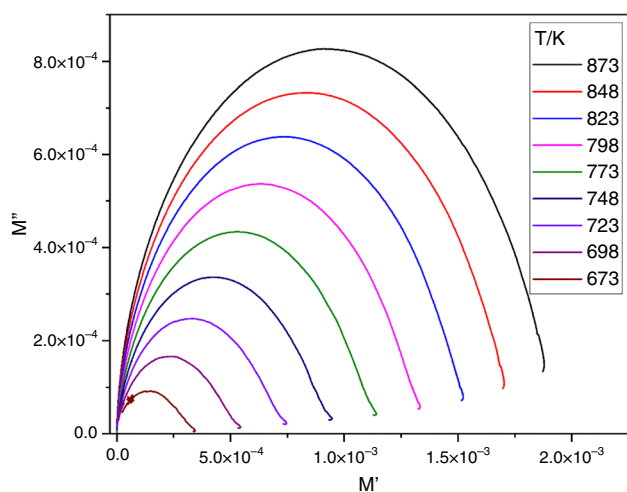

Fig. 18 Cole–Cole plot for the KNN:Eu0.025–1100 sample at selected temperatures

polarization vectors can be rotated more easily by external electric fields.

Conclusions

KNN ceramics powders were prepared by means of a modified Pechini method utilizing citric acid. The effect of doping KNN ceramics with two different amounts of Eu_2O_3 (0.025 or 0.05 mol%) and sintering the obtained powders at two different temperatures (1373 K or 1473 K) was assessed in this work. The structure, microstructure, and dielectric as well as spectroscopic properties of the sinters were studied. A small addition of Eu_2O_3 slightly improved the microstructural parameters of KNN ceramics. When the amount of Eu_2O_3 dopant increased, the points at which phase
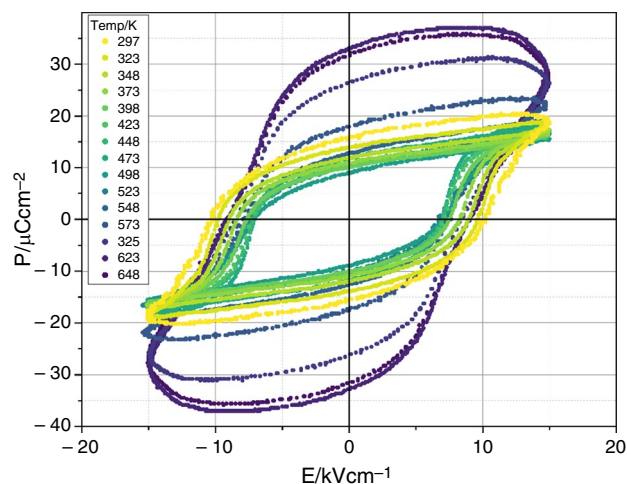
Fig. 19 Hysteresis loops of the KNN:Eu0.025–1100 ceramics measured at temperatures in the range from 300 to 648 K, and with 25 K step
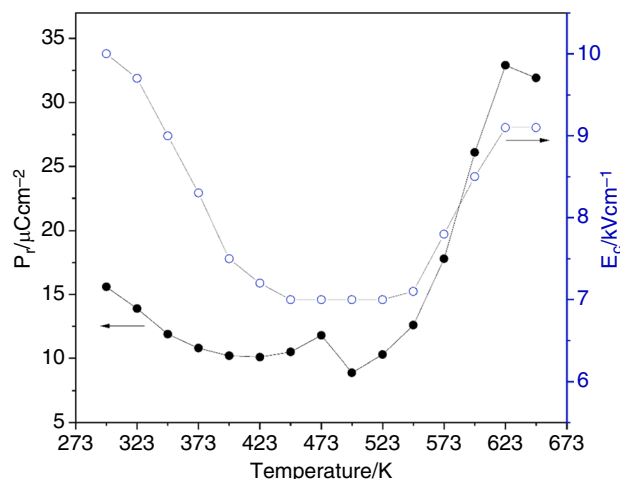

Fig. 20 Temperature dependence of remanent polarization (P_r) and coercive field (E_c) for KNN:Eu0.025–1100

transitions occur shifted toward lower temperature. When the sample was sintered at 1473 K, a liquid phase precipitated, promoting significant grain growth as well as sodium and potassium segregation. This led to the formation of two different phases in the investigated sinters. The presence of these phases induces a transition from a 'normal' phase to a diffuse one and causes the electrical properties to grow worse. The sample that was found to exhibit the optimal physicochemical values was the KNN:Eu0.025–1100 sinter.

References

1. Saito Y, Takao H, Tani T, Nonoyama T, Takatori K, Homma T, Nagaya T, Nakamura M. Lead-free piezoceramics. Nature. 2004;432:84–7. https://doi.org/10.1038/nature03028.

2. Rödel J, Jo W, Seifert KTP, Anton EM, Granzow T, Damjanovic D. Perspective on the development of lead-free piezoceramics. J Am Ceram Soc. 2009;92:1153–77. https://doi.org/10.1111/J.1551-2916.2009.03061.X.

3. Zhang S, Xia R, Shrout TR. Lead-free piezoelectric ceramics vs. PZT? J Electroceramics. 2007;19:251–7. https://doi.org/10.1007/s10832-007-9056-z.

4. Wu J, Xiao D, Zhu J. Potassium-sodium niobate lead-free piezoelectric materials: past, present, and future of phase boundaries. Chem Rev. 2015;115:2559–95.

5. Li JF, Wang K, Zhu FY, Cheng LQ, Yao FZ. (K, Na)NbO3-based lead-free piezoceramics: fundamental aspects, processing technologies, and remaining challenges. J Am Ceram Soc. 2013;96:3677–96. https://doi.org/10.1111/JACE.12715.

6. Hao J, Xu Z, Chu R, Li W, Du J. Bright reddish-orange emission and good piezoelectric properties of Sm 2 O 3-modified (K 05 Na 05)NbO 3-based lead-free piezoelectric ceramics. J Appl Phys. 2015;117:194104. https://doi.org/10.1063/1.4921451.

7. Wu X, Lu S, Kwok KW. Photoluminescence, electro-optic response and piezoelectric properties in pressureless-sintered Er-doped KNN-based transparent ceramics. J Alloys Compd. 2017;695:3573–8. https://doi.org/10.1016/j.jallcom.2016.11.409.

8. Wang J, Luo L, Huang Y, Li W. Effect of Yb codoping on the phase transition, and electrical and photoluminescence properties in KNLN:Er/ x Yb ceramics. J Am Ceram Soc. 2016;99:1625–30. https://doi.org/10.1111/jace.14137.

9. Zhai Y, Du J, Chen C, Li W, Hao J. The photoluminescence and piezoelectric properties of Eu2O3 doped KNN-based ceramics. J Alloys Compd. 2020. https://doi.org/10.1016/j.jallcom.2020.154518.

10. Li W, Hao J, Fu P, Du J, Li P, Li H, Yue Z. High-temperature and long-term stability of Ho-doped potassium sodium niobate-based multifunctional ceramics. Ceram Int. 2021;47:13391–401. https://doi.org/10.1016/j.ceramint.2021.01.196.

11. Wen R, Zhou L, Zou X, Luo L, Jiang N, Zheng Q, Liao J, Xu C, Lin D. Phase transition, electrical and luminescent properties of Dy-doped K0.5Na0.5NbO3-based lead-free ceramics. J Mater Sci Mater Electron. 2015;26:8341–9. https://doi.org/10.1007/s10854-015-3500-7.

12. Wu X, Lau CM, Kwok KW. Effect of phase transition on photoluminescence of Er-doped KNN ceramics. J Lumin. 2014;155:343–50. https://doi.org/10.1016/j.jlumin.2014.07.005.

13. Peddigari M, Dobbidi P. Raman, dielectric and variable range hopping nature of Gd2O3-doped K0.5N0.5NbO3 piezoelectric ceramics. AIP Adv. 2015;5:107129. https://doi.org/10.1063/1.4934676.

14. Du J, Xu Z, Chu R, Hao J, Li W, Jiang G, Zheng P. Rare-earth doped (K0.5Na0.5)NbO3 multifunctional ceramics. J Mater Sci Mater Electron. 2017;28:5288–94. https://doi.org/10.1007/s10854-016-6186-6.

15. Zhai Y, Feng Y, Du J, Xue J, Shen J, Lu Y, Lu T, Fu P, Li W, Hao J, Xu Z. The impedance, dielectric and piezoelectric properties of Tb4O7 and Tm2O3 doped KNN ceramics. J Mater Sci Mater Electron. 2019;30:4352–8. https://doi.org/10.1007/s10854-019-00748-9.

16. Wu X, Lin J, Chen P, Liu C, Lin M, Lin C, Luo L, Zheng X. Ho3+-doped (K, Na)NbO3-based multifunctional transparent ceramics with superior optical temperature sensing performance. J Am Ceram Soc. 2019;102:1249–58. https://doi.org/10.1111/jace.15967.

17. Wang H, Deng B, Lin C, Wu X, Cheng Y, Lin T, Zheng X, Yu X. Noncontact temperature-dependent fluorescence depicting phase transition in Nd3+-doped (K0.5Na0.5)NbO3 ceramics. J Am Ceram Soc. 2020;103:784–9. https://doi.org/10.1111/jace.16872.

18. Sun H, Zhang Y, Liu J, Peng D, Zhang Q, Hao X. Reversible upconversion switching for Ho/Yb codoped (K, Na)NbO3 ceramics with excellent luminescence readout capability. J Am Ceram Soc. 2018;101:5659–74. https://doi.org/10.1111/jace.15885.

19. Zhang Q, Tang J, Du P, Li W, Yuan G, Liu Z, Luo L. Reversible and color controllable emissions in Er3+/Pr3+-codoped K0.5Na0.5NbO3 ceramics with splendid photochromic properties for anti-counterfeiting applications. J Eur Ceram Soc. 2021;41:1904–16. https://doi.org/10.1016/j.jeurceramsoc.2020.10.048.

20. Jia Q, Zhang Q, Sun H, Hao X. High transmittance and optical storage behaviors in Tb3+ doped K0.5Na0.5NbO3-based ferroelectric materials. J Eur Ceram Soc. 2021;41:1211–20. https://doi.org/10.1016/j.jeurceramsoc.2020.10.035.

21. Wei Y, Wu Z, Jia Y, Wu J, Shen Y, Luo H. Dual-enhancement of ferro-/piezoelectricand photoluminescent performance in Pr3+doped (K0.5Na0.5)NbO3 lead-free ceramics. Appl Phys Lett. 2014;105:42902. https://doi.org/10.1063/1.4891959.

22. Wu X, Kwok KW, Li F. Upconversion fluorescence studies of sol-gel-derived Er-doped KNN ceramics. J Alloys Compd. 2013;580:88–92. https://doi.org/10.1016/j.jallcom.2013.05.096.

23. Kumar P, Pattanaik M, Sonia. Synthesis and characterizations of KNN ferroelectric ceramics near 50/50 MPB. Ceram Int. 2013;39:65–9. https://doi.org/10.1016/j.ceramint.2012.05.093.

24. Zhang F, Han L, Bai S, Sun T, Karaki T, Adachi M. Hydrothermal synthesis of (K, Na)NbO3 particles. Jpn J Appl Phys. 2008;47:7685–8. https://doi.org/10.1143/JJAP.47.7685/XML.

25. Shi G, Wang J, Wang H, Wu Z, Wu H. Hydrothermal synthesis of morphology-controlled KNbO3, NaNbO3, and (K, Na)NbO3 powders. Ceram Int. 2017;43:7222–30. https://doi.org/10.1016/j.ceramint.2017.03.012.

26. Bai S, Karaki T. Two-step synthesis of platelike potassium sodium niobate template particles by hydrothermal method. J Am Ceram Soc. 2013;96:2515–8. https://doi.org/10.1111/jace.12345.

27. Chowdhury A, Bould J, Zhang Y, James C, Milne SJ. Nano-powders of Na0.5K0.5NbO3 made by a sol-gel method. J Nanoparticle Res. 2010;12:209–15. https://doi.org/10.1007/S11051-009-9595-0/FIGURES/5.

28. Stavber G, Malič B, Kosec M. A road to environmentally friendly materials chemistry: low-temperature synthesis of nanosized K0.5Na0.5NbO3 powders through peroxide intermediates in

water. Green Chem. 2011;13:1303–10. https://doi.org/10.1039/c0gc00750a.

29. Kumar S, Shandilya M, Thakur S, Thakur N, Anit KG. Effect of sol–gel synthesis method on the structural, electrical, and ferroelectric properties of lead-free K0.5Na0.5NbO3 ceramic. J Sol-Gel Sci Technol. 2019;92:215–23. https://doi.org/10.1007/s10971-019-05077-1.

30. Kakimoto KI, Hayakawa Y, Kagomiya I. Low-temperature sintering of dense (Na, K)NbO3 piezoelectric ceramics using the citrate precursor technique. J Am Ceram Soc. 2010;93:2423–6. https://doi.org/10.1111/j.1551-2916.2010.03748.x.

31. Chowdhury A, O'Callaghan S, Skidmore TA, James C, Milne SJ. Nanopowders of Na0.5K0.5NbO3 prepared by the pechini method. J Am Ceram Soc. 2009;92:758–61. https://doi.org/10.1111/j.1551-2916.2009.02950.x.

32. Lubszczyk M, Brylewski T, Rutkowski P, Świerczek K, Kruk A. Preparation and physicochemical properties of K0.5Na0.5NbO3 ceramics obtained using a modified wet chemistry method. Mater Sci Eng B. 2023;288:116135. https://doi.org/10.1016/j.mseb.2022.116135.

33. Lubszczyk M, Madej D, Brylewski T, Kruk A. Improvements of physicochemical properties of K0.5Na0.5NbO3 ceramics by addition of selected chelating agents. Ceram Int. 2023;49:23045–56. https://doi.org/10.1016/j.ceramint.2023.04.130.

34. Ribeiro de Mesquita B, Marcos MV, Couto dos Santos MA. Theoretical and computational investigation of the Eu3+ ion local symmetry in fluorides compounds. J Lumin. 2021;238:118297. https://doi.org/10.1016/j.jlumin.2021.118297.

35. Hardy A, Van Werde K, Vanhoyland G, Van Bael MK, Mullens J, Van Poucke LC. Study of the decomposition of an aqueous metal-chelate gel precursor for (Bi, La)4Ti3O12 by means of TGA-FTIR. TGA-MS and HT-DRIFT Thermochim Acta. 2003;397:143–53. https://doi.org/10.1016/S0040-6031(02)00272-1.

36. Li W, Zhang W, Shi L, Wang Y, Tan Y, An R, Tsubaki N. Highly active SiO2-supported Cu-ZnO catalysts prepared by combustion methods for low-temperature methanol synthesis: comparative activity test with or without SiO2support. J Japan Pet Inst. 2015;58:321–8. https://doi.org/10.1627/jpi.58.321.

37. Banerjee S, Kumar A, Sujatha DP. Preparation of nanoparticles of oxides by the citrate-nitrate process: effect of metal ions on the thermal decomposition characteristics. J Therm Anal Calorim. 2011;104:859–67. https://doi.org/10.1007/s10973-011-1525-6.

38. Hennings D, Mayr W. Thermal decomposition of (BaTi) citrates into barium titanate. J Solid State Chem. 1978;26:329–38. https://doi.org/10.1016/0022-4596(78)90167-6.

39. Kumada N, Kinomura N. Preparation and crystal structure of K6Nb10.9O30. Eur J solid state Inorg Chem. 1997;32:65–72. https://doi.org/10.1002/chin.199724012.

40. Song HC, Cho KH, Park HY, Ahn CW, Nahm S, Uchino K, Park SH, Lee HG. Microstructure and piezoelectric properties of (1–x)(Na0.5K0.5)NbO3–xLiNbO3 ceramics. J Am Ceram Soc. 2007;90:1812–6. https://doi.org/10.1111/J.1551-2916.2007.01698.X.

41. Wang Y, Damjanovic D, Klein N, Hollenstein E, Setter N. Compositional inhomogeneity in Li- and Ta-modified (K, Na)NbO 3 ceramics. J Am Ceram Soc. 2007;90:3485–9. https://doi.org/10.1111/j.1551-2916.2007.01962.x.

42. Zhen Y, Li JF. Normal sintering of (K, Na)NbO3-based ceramics: Influence of sintering temperature on densification, microstructure, and electrical properties. J Am Ceram Soc. 2006;89:3669–75. https://doi.org/10.1111/j.1551-2916.2006.01313.x.

43. Reisman A, Holtzberg F. Phase equilibria in the system K2CO3-Nb2O5 by the method of differential thermal analysis. J Am Chem Soc. 1955;77:2115–9. https://doi.org/10.1021/ja01613a025.

44. Reisman A, Holtzberg F, Banks E. Reactions of the group VB pentoxides with alkali oxides and carbonates VII heterogeneous equilibria in the system Na 2 O or Na 2 CO 3 -Nb 2 O 5. J Am Chem Soc. 1958;80:37–42. https://doi.org/10.1021/ja01534a011.

45. Fang J, Wang X, Zuo R, Tian Z, Zhong C, Li L. Narrow sintering temperature window for (K, Na)NbO 3-based lead-free piezoceramics caused by compositional segregation. Phys Status Solidi Appl Mater Sci. 2011;208:791–4. https://doi.org/10.1002/PSSA.201026500.

46. Haugen AB, Madaro F, Bjørkeng LP, Grande T, Einarsrud MA. Sintering of sub-micron K0.5Na0.5NbO3 powders fabricated by spray pyrolysis. J Eur Ceram Soc. 2015;35:1449–57. https://doi.org/10.1016/j.jeurceramsoc.2014.11.011.

47. Bah M, Giovannelli F, Retoux R, Bustillo J, Le CE, Monot-Laffez I. Crystal growth and piezoelectric properties of lead-free based K0.5Na0.5NbO3 by the floating zone method. Cryst Growth Des. 2016;16:315–24. https://doi.org/10.1021/acs.cgd.5b01271.

48. Skidmore TA, Milne SJ. Phase development during mixed-oxide processing of a [Na0.5K0.5NbO3]1−x–[LiTaO3]x powder. J Mater Res. 2007;22:2265–72. https://doi.org/10.1557/JMR.2007.0281.

49. Baker DW, Thomas PA, Zhang N, Glazer AM. Structural study of Kx Na1 - X NbO3 (KNN) for compositions in the range x = 0.24–0.36. Acta Crystallogr Sect B Struct Sci. 2009;65:22–8. https://doi.org/10.1107/S0108768108037361.

50. Shannon RD. Revised effective ionic radii and systematic studies of interatomic distances in halides and chalcogenides. Acta Crystallogr Sect A. 1976;32:751–67. https://doi.org/10.1107/S0567739476001551.

51. Ahn CW, Park CS, Choi CH, Nahm S, Yoo MJ, Lee HG, Priya S. Sintering behavior of lead-free (K, Na)NbO3-basedpiezoelectric ceramics. J Am Ceram Soc. 2009;92:2033–8. https://doi.org/10.1111/j.1551-2916.2009.03167.x.

52. Wang X, Huan Y, Wang Z, Lin X, Huang S, Wei T, Li L, Wang X. Electrical conduction and dielectric relaxation mechanisms in the KNN-based ceramics. J Appl Phys. 2019;126: 104101. https://doi.org/10.1063/1.5110582.

53. Rayssi C, El Kossi S, Dhahri J, Khirouni K. Frequency and temperature-dependence of dielectric permittivity and electric modulus studies of the solid solution Ca0.85Er0.1Ti1-: XCo4 x /3O3 (0 ≤ x ≤ 0.1). RSC Adv. 2018. https://doi.org/10.1039/c8ra00794b.

54. Wang Y, Pu Y, Zhang P. Investigation of dielectric relaxation in BaTiO3 ceramics modified with BiYO3 by impedance spectroscopy. J Alloys Compd. 2015. https://doi.org/10.1016/j.jallcom.2015.09.012.